Available online at www.sciencedirect.com
SCIENCE DIRECT®
Applied Clay Science 27 (2004) 29–40
Applied CLAY Science
www.elsevier.com/locate/clay

Structural and photooxidation properties of SnO_2/layer silicate nanocomposites

László Kőrösi[a], József Németh[a], Imre Dékány[a,b,*]

[a] *Department of Colloid Chemistry, University of Szeged, H-6720 Szeged, Aradi v. t. 1, Hungary*
[b] *Nanostructured Materials Research Group of Hungarian Academy of Sciences, University of Szeged, H-6720 Szeged, Aradi v. t. 1, Hungary*

Received 26 May 2003; received in revised form 17 November 2003; accepted 4 December 2003
Available online 28 February 2004

Abstract

SnO_2 nanoparticles were prepared by hydrolysis in aqueous medium and stabilized by montmorillonite or hectorite. The tin content of SnO_2/clay nanocomposites varied between 15 and 50 wt.%. Intercalation of tin dioxide nanoparticles between the lamellae of the minerals was verified by X-ray diffraction. Calcination temperature of the samples was changed in the range of 80–1000 °C. It was shown by N_2 gas adsorption measurements that as temperature was increased, the specific surface area of the catalysts (80–210 m^2/g) markedly decreased. The presence of SnO_2 particles measuring 2–6 nm was verified by transmission electron microscopy, atomic force microscopy, X-ray diffraction, dynamic light scattering. The photooxidative efficiency of SnO_2/clay photocatalysts was investigated by degradation of salicylic acid. It was established that the catalytic effect is mainly due to the presence of nanosized tin dioxide particles. By selecting the appropriate experimental conditions, we accomplished size-controlled synthesis of nanocrystalline tin dioxide surpassing microcrystalline SnO_2 in catalytic activity.

Keywords: Tin dioxide; Layer silicates; Montmorillonite; Hectorite; Adsorption; Intercalation; Nanoparticles; Photocatalysis

1. Introduction

Over the past decades, many successful attempts on the generation of size quantized semiconductor particles have been reported (Ozin, 1992; Weller, 1993). Metal oxide nanoparticles with controllable pore structure and particle size have gained increasing importance (Richards et al., 2000). Tin dioxide, a material with versatile applicability in a large number of physico-chemical procedures is one of the most intensively studied semiconductors. As an n-type semiconductor, it is extremely sensitive to reducing gases (CO, H_2, ethanol, hydrocarbons) and may therefore be made use of as a gas sensor (Ansari et al., 1997, 2002; Maffeis et al., 2002; Salehi, 2002). Due to its photocatalytic properties, it may be put to use in the degradation of organic molecules in aqueous medium (Cun et al., 2002; Serpone and Salinaro,

Abbreviations: SnO_2/Mont/H/14.3, Mont: sodium montmorillonite, or Hect: sodium hectorite layer silicate support; H, preparation by heterocoagulation; 14.3, the SnO_2 content in wt.%.

* Corresponding author. Department of Colloid Chemistry, University of Szeged, H-6720 Szeged, Aradi v. t. 1, Hungary. Fax: +36-62-312-921.
E-mail address: i.dekany@chem.u-szeged.hu (I. Dékány).

0169-1317/$ - see front matter © 2003 Elsevier B.V. All rights reserved.
doi:10.1016/j.clay.2003.12.004

1999; Sukharev and Kershaw, 1996; Vinodgopal and Kamat, 1995; Yumoto et al., 1999), a problem often encountered in environmental protection (Hagfeldt and Graetzel, 1995). It is also widely used as substrate for the construction of electrodes (Chappel and Zaban, 2002; Santos-Pena et al., 2000). The favourable properties of tin dioxide are closely linked to particle size. There are numerous physical and chemical methods available for the preparation of the particles at the lower limits of the colloid size range. One of the methods to achieve this goal is gas-phase condensation (Jiménez et al., 1996, 1999). Colloid chemical methods presently applied to produce tin dioxide nanoparticles include the use of reversed micelles (or microemulsions) (Kim et al., 1999; Song and Kim, 1999). Consumption of expensive and environmentally unfriendly organic solvents and surfactants are the disadvantages of using reversed micelles. Therefore, efforts have been made to develop a hydrothermal procedure for the synthesis of tin dioxide nanoparticles (Nütz and Haase, 2000; Richards et al., 2000) and using inexpensive stabilizing agents and environmental friendly materials, e.g. layer silicates (Dékány et al., 1999, 2000; Kiricsi et al., 1994). The interlamellar distance of the layer silicates makes possible the preparation of particles of a well-defined size (3–6 nm) (Dékány et al., 1995). The method involves coagulation of a sol with positive surface charge and a layer silicate suspension with negative surface charge, this method is known as heterocoagulation (Ding et al., 1999; Mogyorósi et al., 2003; Ooka et al., 1999; Yamanaka et al., 1987).

In the present work, the preparation of clay stabilized SnO_2 nanoparticles and their application for the photooxidative degradation of organic molecules is studied. The relationship between the structural properties and the photooxidation ability is also examined.

2. Experimental procedures

2.1. Materials

For the preparation of semiconductor/layer silicate composites, tin(IV) chloride pentahydrate (minimum purity 98%, Aldrich Chem.), Na-montmorillonite (ion-exchanged, sedimented, $d<2$, Wyoming, USA) and synthetic hectorite (Optigel SH Süd-Chemie) were used. Chemicals utilized in the course of the analysis of nanocomposites were sodium hydroxide, concentrated sulphuric acid, citric acid monohydrate, trisodium citrate, hydrogen peroxide, absolute methanol (Reanal, Hungary), phenylfluorone (9-phenyl-2,6,7-trihydroxy-3-fluorone) (Fluka) and gum arabic. The photooxidative efficiency of SnO_2/layer silicate nanocomposites and the reference, tin dioxide (99.99%, Aldrich) was determined with salicylic acid (Reanal) as test molecule.

2.2. Sample preparation

$Sn(OH)_4$ hydrosols were prepared by hydrolysis of $SnCl_4$ using the following procedure: 4.75 g of $SnCl_4 \times 5\ H_2O$ and 1.06 g of NaOH were dissolved into 50.0-ml distilled water each. The alkali solution was added dropwise to the intensively stirred tin(IV) chloride solution and the mixture was homogenized by sonication for 5 min. For the preparation of nanocomposites, tin(IV) hydroxide sol (water/sol 1:1, $c_{Sn(OH)_4} \sim 3.3 \times 10^{-2}$ mol dm^{-3}) was used. Tin dioxide nanoparticles were delivered to the interlamellar space by heterocoagulation, when different amounts of $Sn(OH)_4$ sol were added to 1% (w/v) montmorillonite or hectorite suspensions under constant stirring (Fig. 1). The resulting $Sn(OH)_4$/layer silicate nanocomposite suspensions were centrifuged for 15 min at 3500 min^{-1}. The sediment was redispersed in ca. 400-ml distilled water, washed and recentrifuged. The preparation was washed three times in distilled water and once in ethanol, dried at 80 °C and ground to a fine powder in an agate mortar. The samples were calcinated in a tube furnace (heating rate 5 °C/min) for 3 h at 400 °C. Heat treatments of a selected catalyst, sample SnO_2/Hect/H/50.3 were carried out for 3 h at 80–1000 °C.

2.3. Extraction of SnO_2/layer silicate composites and determination of their tin content

Tin dioxide is not fully soluble in concentrated mineral acids. Full extraction was achieved by sodium hydroxide fusion (800 °C). Four grams (for supported samples, 6 g) of NaOH was added to a nickel crucible, heated with a Bunsen burner and kept in a melted state until the end of vapour formation, then kept at dull red heat (ca. 800 °C) for 2 min. Powdered tin-containing

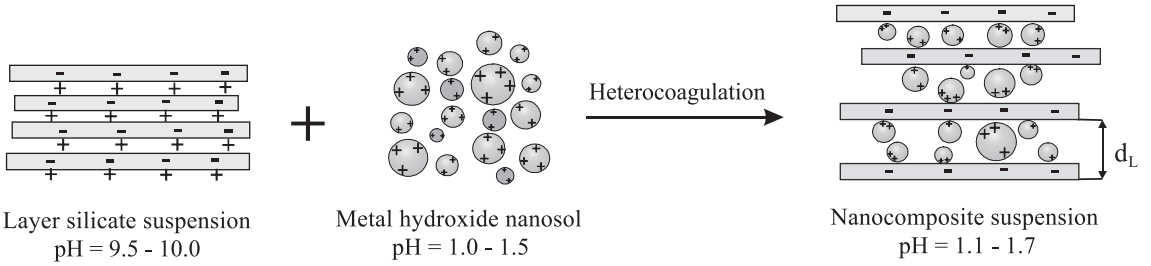

Fig. 1. Schematic illustration of the heterocoagulation process between layer silicate and metal hydroxide nanosol particles.

sample (0.1–0.2 g) was next sprinkled on the melt, the crucible was covered and heated for 5 min at ca. 800 °C. After cooling, the crucible and its lid were heated to about 80 °C in 150 ml of distilled water in a 250-ml beaker. The contents of the beaker were next transferred to a 500-ml volumetric flask and 30 ml of concentrated sulphuric acid was carefully added in small portions, as a result of which the solution cleared up completely. In acidic medium, Sn^{4+} forms an orange complex ($\lambda_{max} = 510$ nm) with phenylfluorone (9-phenyl-2,6,7-trihydroxy-3-fluorone), which can only be maintained in a state suitable for photometric determination with the help of a protective colloid (e.g. gum arabic) (Smith, 1970). For photometry, tin(IV) solutions with different concentrations were made up by dissolving metallic tin in concentrated sulphuric acid. Light absorption of the samples was measured after 2 h (i.e. the time necessary for full colour development) at 510 nm, using a reference solution that contained all components except for Sn^{4+} ions. The tin content of the samples was determined with the help of a calibration curve (straight line).

2.4. Photooxidation studies

Photocatalytical experiments were made in a 400-ml batch reactor, thermostated at 25 ± 0.1 °C and equipped with an immersion-type UV lamp (high-pressure mercury lamp, 150 W, $\lambda = 240–580$ nm). In our experiments, the surrounding of the lamp with a glass filter allowed a considerable proportion of the high-energy photons ($\lambda < 310$ nm) to be filtered out. In order to test the catalytic efficiency of photocatalyst nanocomposites, the photooxidative degradation of salicylic acid was studied. A 0.1% (w/v) SnO_2/layer silicate suspension was made up in 0.15 mmol dm^{-3} salicylic acid solution. During a 1-h irradiation, samples were withdrawn after 5, 10, 20, 30, 40, 50 and 60 min.

Analysis of the organic content of the samples after photooxidation was carried out using an UVIKON 930 UV–VIS dual-beam spectrophotometer.

2.5. Measurement methods

The average particle diameter (d_{DLS}) of the prepared tin oxide/hydroxide nanosols was determined by SEMATech 633 (France) dynamic light scattering (DLS) apparatus (He–Ne laser, 5 mW).

The streaming potential examinations of the colloidal dispersions were accomplished using a Mütek PCD 02 particle charge detector with Au electrodes (Mütek Analytic, Germany).

The specific surface area of samples were determined by a Micromeritics Gas Adsorption Analyzer (Gemini Type 2375) at 77 ± 0.5 K in liquid nitrogen. Prior to measurements the samples were pretreated in a vacuum at 120 °C for 2 h. The sample vessel was loaded with ca. 0.1–0.7 g of samples. The adsorption isotherms were analyzed by means of the BET equation.

X-ray diffraction measurements were performed on a Philips PW 1820/1830 diffractometer, (CuKα = 0.1542 nm, 40 kV, and 30 mA, in the 1–30° (2Θ) regime for solid powder samples). The basal distances, d_L, were calculated from the first (001) Bragg reflections by using the PW 1877 automated powder diffraction software. The standard deviation of the d_L values was established to be ± 0.01 nm in the 1–10° (2Θ) range, and ± 0.001 nm in the 20–30° (2Θ) range. The average diameters of the particles (D) were obtained by means of the Scherrer equation [$D = k\alpha/\beta\cos\Theta$, where β = line broadening ($\beta = \beta_s - \beta_0$, where β_s and β_0 the

half-widths of the XRD peak of the sample and of the silicon standard], k is related to the crystallite shape, and α and Θ are the radiation wavelength and Bragg angle, respectively) (Bartram, 1967). A single crystal silicon standard ($\beta_0 = 0.105°$, 2Θ) was used for calibration.

Transmission electron microscopy (TEM) images of the applied nanosols were taken using a Philips CM-10 electron microscope, using an accelerating voltage of 100 kV. The samples were dispersed in ethanol and the aliquots were dropped on a 2-mm diameter Formvar-coated copper grids. The particle size distribution was determined by using UTHSCSA Image Tool program.

A NanoScope III Multimode Atomic Force Microscope (Digital Instruments, USA) was used to obtain topographic information about the nanoparticles using a small scanner (x,y: 12 μm; z: 3 μm). The tapping mode images were scanned with an etched silicon tapping mode tip (length of cantilever 125 μm, RTESP tips from Veeco).

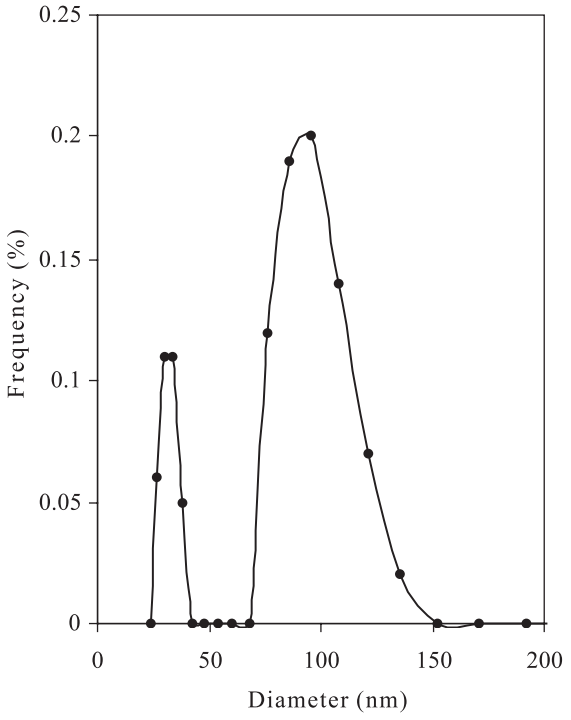

Fig. 2. Particle size distribution function of tin hydroxide nanosol obtained by DLS measurement.

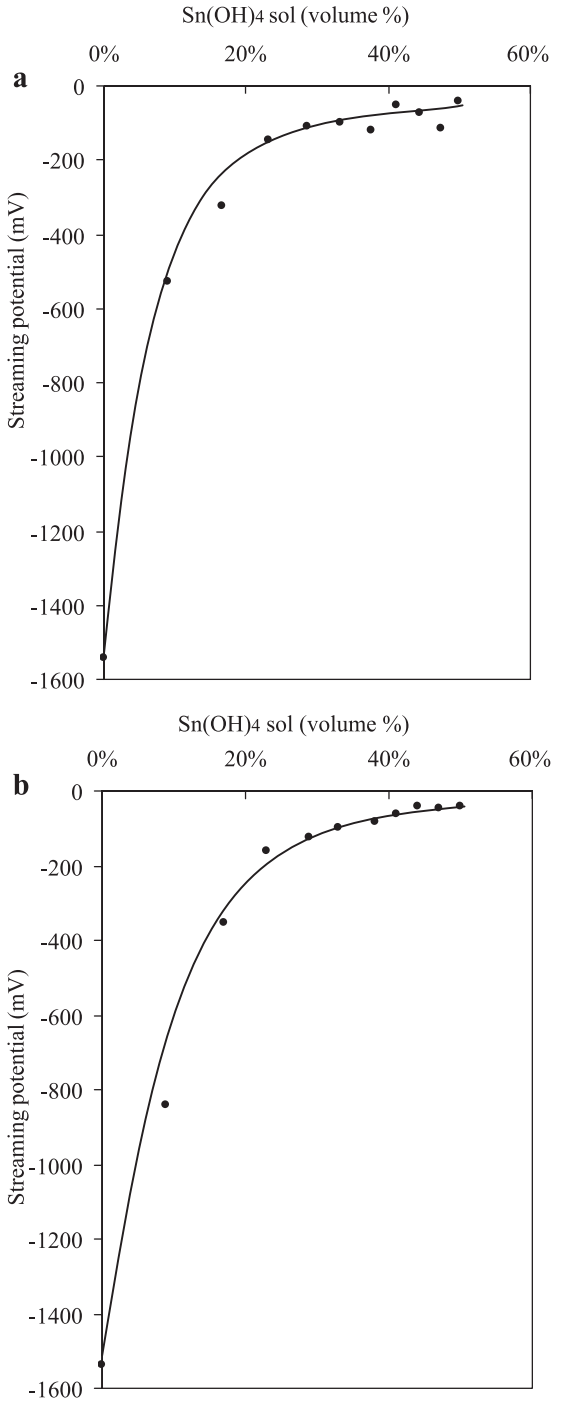

Fig. 3. (a) Titration of 1 w/v% aqueous montmorillonite suspension by 0.6 w/v% tin hydroxide sol. (b) Titration of 1 w/v% aqueous hectorite suspension by 0.6 w/v% tin hydroxide sol.

3. Results and discussion

3.1. Properties of $Sn(OH)_4$ hydrosols

The size distribution of the sol particles used for nanocomposite preparation was determined by dynamic light scattering (DLS) (Fig. 2). The results show that at pH ~ 1.0 the sol contained particles measuring $d_{av} = 90$ nm that characteristically fell into two size ranges (25–40 and 75–150 nm). At such low pH values, the sol is stable for several hours and particles are not perceived visually. For successful nanocomposite preparation, it is important to know the surface charge of hydrosols, because the procedure is based on the interaction between oppositely charged surfaces. For this reason, a series of dilutions was made of the $Sn(OH)_4$ hydrosol ($c_{Sn(OH)_4} \sim 6.6 \times 10^{-2}$ mol dm^{-3}) with distilled water. The surface charge of these suspensions was determined from streaming potential measurements. Since the most positive surface charge ($\Psi \sim +8$ mV) was measured for the sample with a $Sn(OH)_4$ concentration of about 3.3×10^{-2} mol dm^{-3} (pH = 1.1), this sol was selected for coagulating layer silicates. The streaming potential was also measured in the course of titration with the layer silicate sol. The value of Ψ was about -40 mV when the volume ratio of layer silicate/sol was 1:1. This value was considered as the optimal silicate/sol ratio (Fig. 3a and b). Hydrosols were added to montmorillonite and hectorite suspensions accordingly and composites of appropriate compositions were obtained (Table 1).

The presence of nanoparticles in the sol samples used for synthesis was verified by transmission electron microscopy (Fig. 4a). A particle size distribution function was also constructed by computer evaluation of the TEM images (Fig. 4b). It was established on this basis that the size distribution of the primary particles is relatively uniform; the average particle size is ~ 6 nm. Comparison of this average value with that obtained by DLS indicates aggregation of the primary particles. The aggregates measuring 80–90

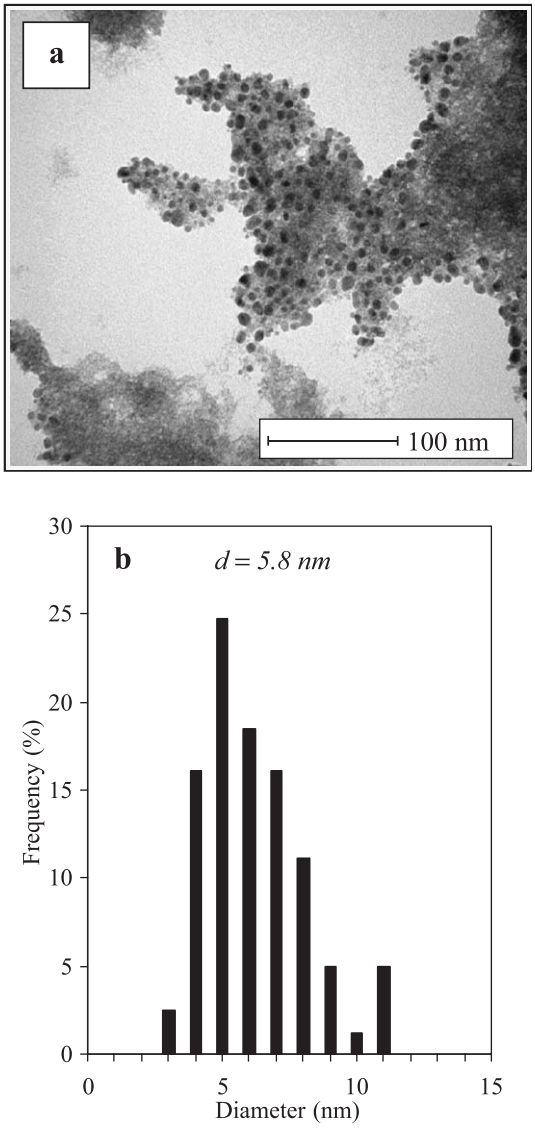

Fig. 4. (a) The TEM image and (b) particle size distribution of $SnO_2 \times nH_2O$ nanoparticles.

Table 1
The basal spacing of SnO_2/layer silicate nanocomposites calcinated at 400 °C

Sample	SnO_2 content (wt.%)	Basal spacing, d_L (nm)
Na-montmorillonite	–	1.0
SnO_2/Mont/H/14.4	14.4	6.6
SnO_2/Mont/H/26.0	26.0	3.5
SnO_2/Mont/H/40.9	40.9	2.7
Na-hectorite	–	1.1
SnO_2/Hect/H/30.6	30.6	6.1
SnO_2/Hect/H/50.3	50.3	3.3

nm in diameter are made up of primary particles with an average size of 4–9 nm.

Nanofilms were prepared on glass surfaces, using $Sn(OH)_4$ hydrosols in aqueous medium. Particle diameters determined by AFM fell into the range of 40–90 nm (Fig. 5a and b), i.e. in this case also aggregates can be seen.

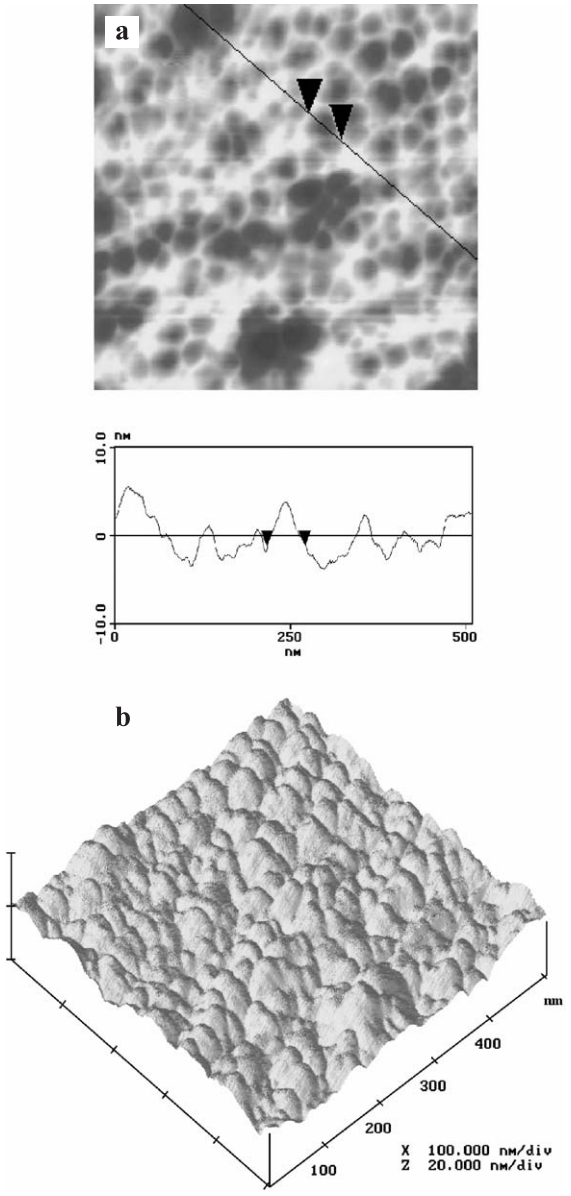

Fig. 5. (a) Cross-section profiles (b) the AFM image of $SnO_2 \times nH_2O$ semiconductor nanoparticles on glass support.

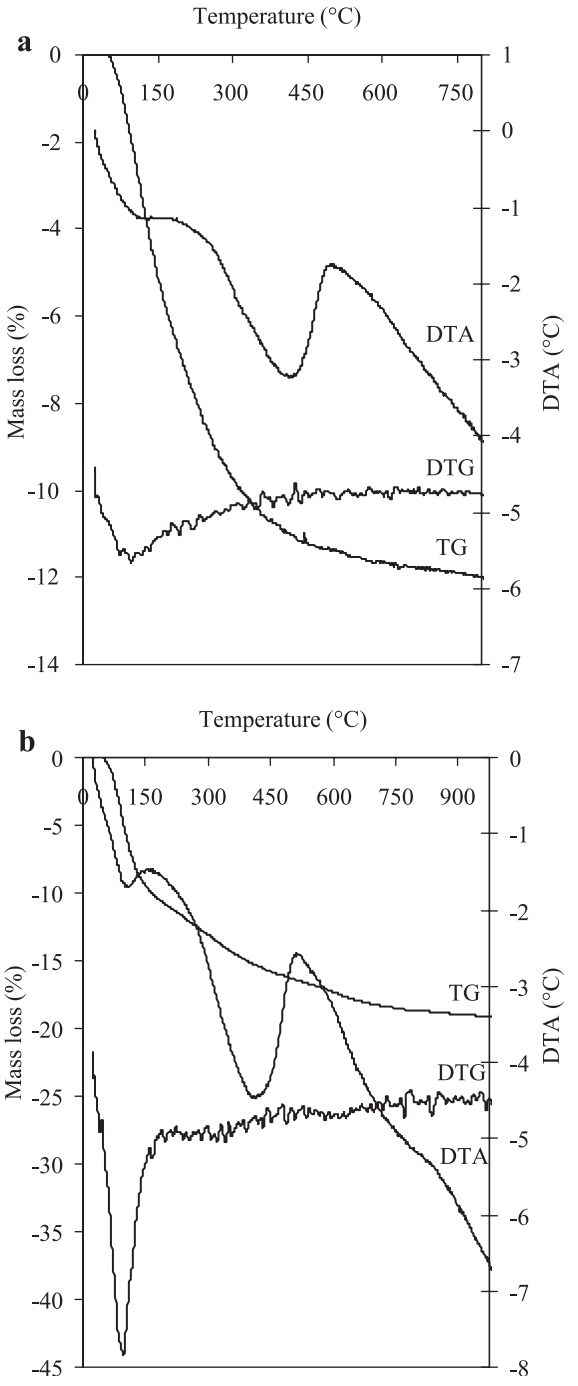

Fig. 6. (a) Thermoanalytical curves of SnO_2 and (b) thermoanalytical curves of SnO_2/Hect/H/50.3 nanocomposite.

3.2. The specific surface area and the porosity of nanocomposites

The SnO_2 and SnO_2/hectorite nanocomposite was subjected to thermoanalytical studies, the results of which are shown in Fig. 6a and b. By the evidence of the DTG curve, the joint dehydration of the metal hydroxide and the mineral takes place between 100 and 190 °C; in the region from 290 to 520 °C, a slight decrease in mass indicates the hydroxide → oxide conversion (minimum at 340 °C). Between 570 and 690 °C, another slight but detectable mass loss signals the dehydroxylation of hectorite (minimum at 630 °C). The above processes may also be recognized in the different regions of the DTA curve. It has to be noted that the second endothermic process is followed by an exothermic one, crystallization of amorphous tin oxide, which may be verified in an independent experiment. The total mass loss of the sample up to 700 °C is 18.2%.

Gas adsorption isotherms of SnO_2/Hect/H/50.3 sample at different temperatures are presented in Fig. 7. The shape of the isotherms is significantly changed by heating and, at the same time, adsorption capacity is drastically reduced. After heating at 150 °C, the specific surface area is still large (200 $m^2 g^{-1}$); at 400 and 600 °C, mesoporous structure develops; finally, in the case of the SnO_2/Hect/H/50.3 sample heated at 800 °C the courses of the adsorption and desorption branches are identical, the pores disappear and the lamellae fully adhere to each other. The gas is condensed into the micropores already at lower pressures, as shown by the higher V^s starting point (adsorbed amount) of the isotherm of the 150 °C sample. In the intermediate temperature range (400–600 °C), the hysteresis loop is considerably larger, indicating mesoporous structure.

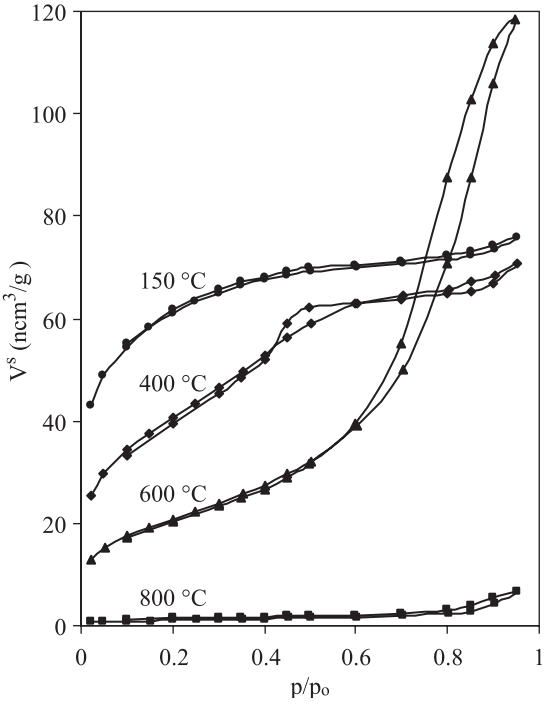

Fig. 7. N_2 adsorption isoterms of SnO_2/Hect/H/50.3 photocatalyst calcinated at different temperatures.

Table 2
The specific surface area of SnO_2/layer silicate nanocomposites calcinated at 400 °C

sample	Surface area, a^s_{BET} (m^2/g)	Micropore surface, a^s_{mp} (m^2/g)	Micropore volume, V^s_{mp} (cm^3/g)
Na-montmorillonite	30.0	2.95	0.00125
SnO_2/Mont/H/14.4	126.8	2.96	0.00017
SnO_2/Mont/H/26.0	121.7	48.56	0.02565
SnO_2/Mont/H/40.9	121.8	3.11	0.00069
Na-hectorite	235.7	21.16	0.00985
SnO_2/Hect/H/30.6	142.3	10.63	0.00501
SnO_2/Hect/H/50.3	137.3	4.95	0.0021

Values of specific surface area (a^s_{BET}) for the samples prepared with different SnO_2 content were determined from N_2 adsorption measurements using the linearized BET equation. In addition, the surface and the volume of micropores (a^s_{mp} and V^s_{mp}, respectively) were also calculated for each sample, using de Boer's *t*-method (Table 2). The data in the table allow

Table 3
The porosity of SnO_2/Hect/H/50.3 SnO_2/hectorite nanocomposites calcinated at different temperatures

Calcination temperature (°C)	Surface area, a^s_{BET} (m^2/g)	Micropore surface (m^2/g)	Micropore volume (cm^3/g)
80	202.7	66.07	0.0355
150	199.9	64.63	0.0348
200	197.0	54.01	0.0289
400	137.3	4.95	0.0021
600	74.8	0	0
800	3.8	0	0
1000	0.7	0	0

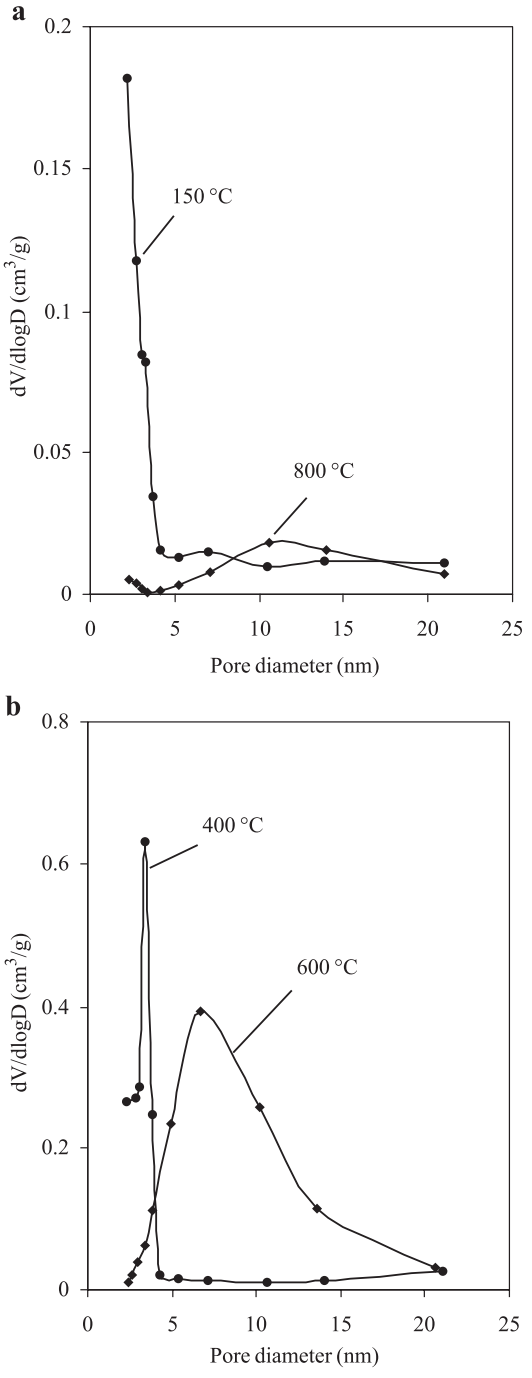

Fig. 8. (a) Differential pore volume distribution functions of SnO_2/Hect/H/50.3 catalyst calcinated at 150 and 800 °C. (b) Differential pore volume distribution functions of SnO_2/Hect/H/50.3 catalyst calcinated at 400 and 600 °C.

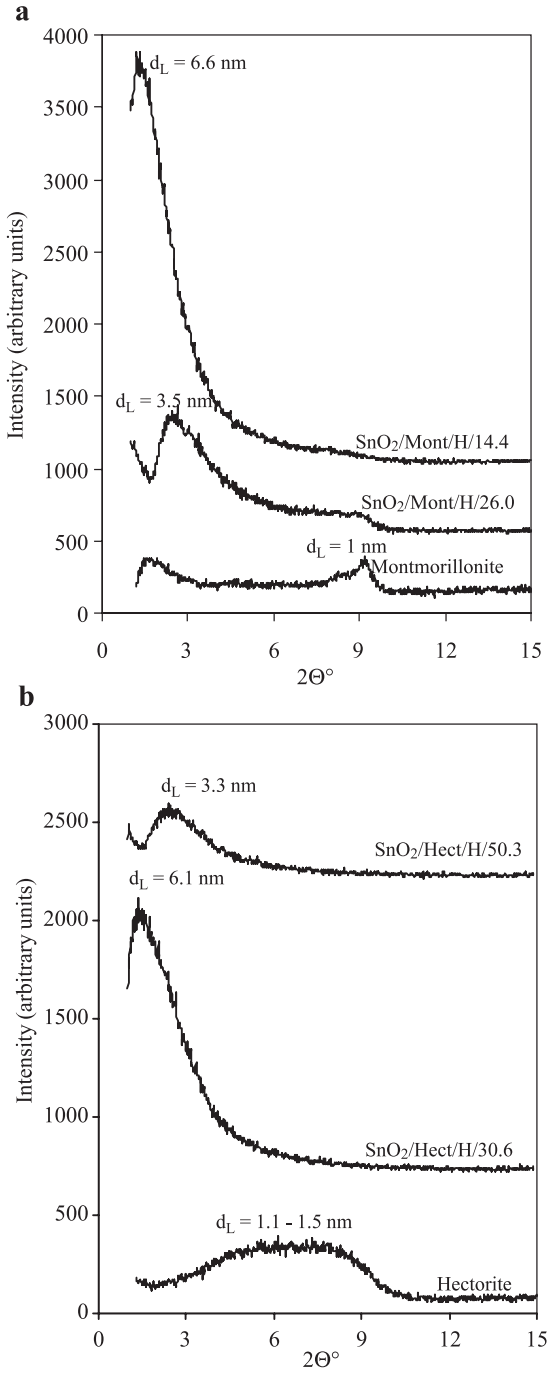

Fig. 9. (a) XRD patterns of SnO_2/montmorillonite nanocomposites containing different amounts of SnO_2 after calcination at 400 °C. (b) XRD patterns of SnO_2/hectorite nanocomposites containing different amounts of SnO_2 after calcination at 400 °C.

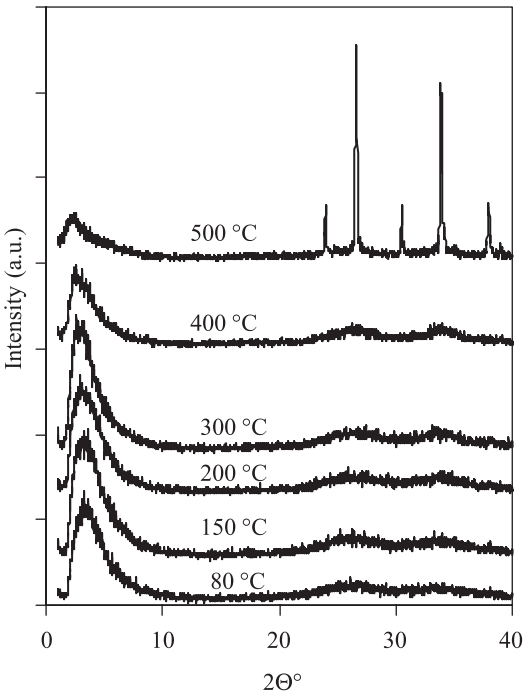

Fig. 10. XRD patterns of SnO_2/Hect/H/50.3 nanocomposite calcinated at different temperatures.

to conclude that the specific surface areas of the samples do not depend significantly on their tin contents. It can be established, however, that the structure of the layer silicate is fundamentally altered by the SnO_2 particles incorporating between the lamellae: there is a ca. 300% increase in specific surface area. Adding acidic tin hydroxide sol (pH = 0.9–1.0) during the preparation of the SnO_2/silicate nanocomposites, Al^{3+} ions are dissolved from the clay layers, ensuring possibility for the formation of a more porous clay structure. In the case of the SnO_2/Mont/H/14.4 and SnO_2/Mont/H/26 catalysts, the pores of the clay particles are filled by the semiconductor nanocrystals formed in the interlamellar space. Probably in the case of the SnO_2/Mont/H/26 catalyst these newly formed pores in the clay sheets are not filled by the nanoparticles, because the crystallites are formed mainly in the bulk phase. The N_2 adsorption measurements also allow the determination of pore size distribution. Our studies on porosity also support the fact that significant structural changes take place as calcination temperature is increased. Another remarkable result of the N_2 adsorption measurements is that the volume and the surface of the pores of the SnO_2/Hect/H/50.3 catalyst—as well as its specific surface area—decrease with increasing calcination temperature, which is due to the increasing size and, later, to the disappearance of pores of the nanometer dimension (2.5–6.5 nm) (Table 3). The differential pore size distributions of the catalysts are presented in Fig. 8a and b.

It is often advantageous if catalysts have large specific surface areas. Another point to be considered is that, due to the $Sn(OH)_4 \rightarrow SnO_2$ conversion, the amount of catalytically active tin dioxide will become significant only at higher temperatures (ca. 400 °C). However, higher temperatures decrease specific the surface area.

3.3. Structure of the SnO_2-layer silicate nanocomposites

Changes occurring in the structure of lamellar supports can be monitored on the basis of Bragg reflections determined from the X-ray diffractograms of the SnO_2/layer silicate samples. For comparison, diffractograms of various composites with different tin dioxide contents calcinated at 400 °C and those of layer silicates without tin dioxide nanoparticles were determined (Fig. 9a and b). The reflections of the powdered samples were studied at $2\Theta = 1–40°$. Reflections at relatively small angles ($2\Theta = 1–15°$) allowed conclusions to be drawn concerning the intercalation of SnO_2, whereas those at larger angles ($2\Theta = 30–40°$) yielded information on the degree of crystallinity of tin dioxide.

The intercalation of nanoparticles alters the original basal spacing of montmorillonite. The decrease in

Table 4
Diameter of tin oxide nanoparticles in SnO_2/Hect/H/50.3 nanocomposite at different calcination temperature

Calcination temperatures (°C)	SnO_2 crystallite size (nm)
80	1.5
150	1.6
200	1.6
300	1.9
400	2.1
500	>100

Table 5
Photochemical composition rate and structural parameters of SnO_2/layer silicate nanocomposites calcinated at 400 °C

Sample	Decomposition (in %, after 1 h)	Basal spacing, d_L (nm)	Surface area, a^s (m^2/g)
SnO_2 (bulk)	15	–	6.0
SnO_2/Mont/H/14.4	45.3	6.6	126.8
SnO_2/Mont/H/26.0	43.0	3.5	121.7
SnO_2/Mont/H/40.9	41.6	2.7	121.8
SnO_2/Hect/H/30.6	76.3	6.1	142.3
SnO_2/Hect/H/50.3	68.5	3.3	137.3

the intensity of the peak corresponding to the basal spacing of the support after calcination at 400 °C ($d_L = 1$ nm) is attributable to the increasing colonization of the interlamellar space by nanoparticles as SnO_2 content increases. Increasing the tin content of the sample also brings about a decrease in basal spacing, because adding more and more $Sn(OH)_4$ sol to the layer silicate suspension the pH of the formed $Sn(OH)_4$/layer silicate disperse system decreases, causing the presence of the smaller semiconductor nanocrystals. The decrease in basal spacing with increasing tin content is also observed in samples with hectorite support (Table 1). Calcination temperature also plays a role in the changes occurring in the

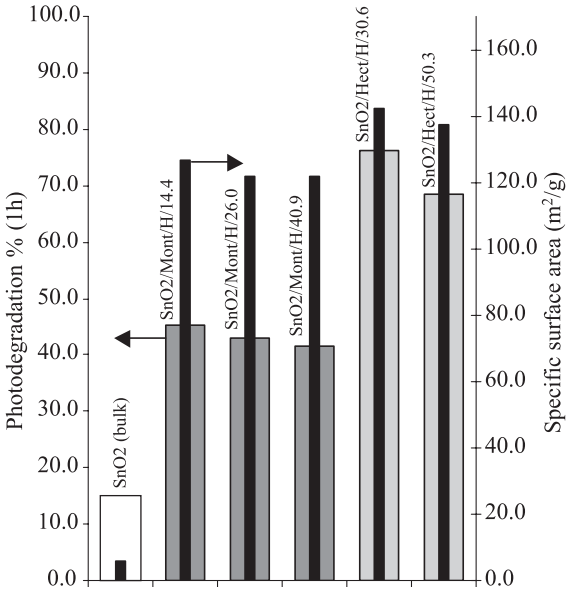

Fig. 11. Photocatalytic activity and specific surface area of the SnO_2/layer silicate nanocomposites calcinated at 400 °C.

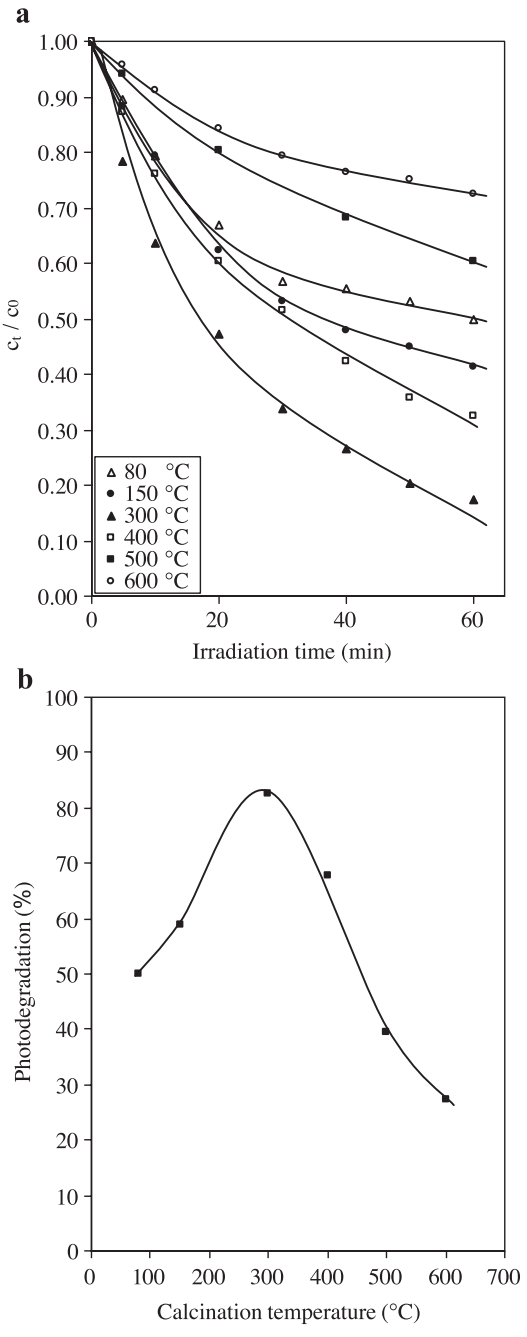

Fig. 12. (a) Photodegradation profiles of salicylic applying SnO_2/Hect/H/50.3 photocatalyst calcinated at different temperatures (initial conc. (c_0) = 0.15 mmol dm^{-3} in 0.1 w/v% suspension of the catalyst). (b) Photodegradation efficiency of SnO_2/Hec/H/50.3 nanocomposite after 1 h of irradiation as the function of the calcination temperature.

structure of layer silicates. The effect of temperature on mineral structure was studied in detail on the SnO_2/Hect/H/50.3 sample (Fig. 10). In samples heated to higher temperatures the intercalation peak is more diffuse, its intensity decreases, whereas the peaks characteristic of SnO_2 appear at progressively increasing intensities and decreasing half widths, indicating structural degradation of the support as well as an increase in the crystallinity of tin dioxide. Particle size calculated by the Scherrer equation varies in the range of 1.5–2.1 nm (Table 4).

3.4. Evaluation of photocatalytic efficiency

The relationship between the photooxidative efficiencies of the catalysts prepared under different conditions and their structural parameters are given in Table 5. The specific surface areas of SnO_2/montmorillonite catalysts calcinated at 400 °C are nearly identical (122–127 m^2 g^{-1}), therefore there is no significant difference between their photooxidative efficiencies, which—according to our measurements—vary in the range of 41–45%. The degradation efficiency of SnO_2/hectorite catalysts is also correlated with the increase in specific surface area (Fig. 11). SnO_2/Hect/H/30.6 sample calcinated at 400 °C has the largest specific surface area showing degradation of 76% after 1 h of irradiation. Thus, it is not the total tin content of the sample that determines photooxidative efficiency: the contribution of the surface of the nanoparticles to the total surface of the sample is more important. The more particles get into the interlamellar space (this depends on their size, their surface charge and the pH), the more pillared the structure becomes (d_L = 3.2–6.6 nm). The increased proportion of nanostructured SnO_2 increases the specific surface area and the formed intercalated structure (see Fig. 1) is also demonstrated by the increased photooxidative efficiency. The assumption that the proportion of nanostructured particles is a decisive factor determining the efficiency of photooxidative degradation was supported by the result of the degradation of the macrocrystal tin dioxide reference sample (Table 5). Calcination temperature of the SnO_2/Hect/H/50.3 catalyst also affects the efficiency of photooxidation via structural changes (Fig. 12a). The optimal calcination temperature of the SnO_2/Hect/H/50.3 nanocomposite is 300 °C, where the catalyst removes more than 82.5% of the test pollutant after 1 h of the irradiation. For interpreting the optimal calcination temperature of 300 °C, it have to be considered, that the amount of the photocatalytically active SnO_2 increases as the result of the tin hydroxide → oxide conversion when the temperature is increased up to 300 °C. The tin hydroxide → oxide conversion up to 520 °C, but the photooxidation efficiency of the nanocomposite from 300 °C due to the enhanced aggregation process taking place between the nanoparticles. As the aggregation of the SnO_2 crystallites proceeds their surface area decreases, causing also a decrease of the photooxidative efficiency. The reason for the higher photooxidative efficiency of hectorite-supported SnO_2 samples compared to the samples containing montmorillonite may be that the optical transparency of hectorite is higher than that of montmorillonite.

4. Conclusions

Nanostructured SnO_2/layer silicate composites were prepared. Nanoparticles were synthesized by simple hydrolysis in aqueous medium and the size stabilization was effected by layer silicates, Na-montmorillonite and Na-hectorite. Correlations between the preparation conditions of the composites and their structure were verified by various methods. Intercalation of tin dioxide nanoparticles was unambiguously proven by X-ray diffraction. The effect of calcination temperature was followed by monitoring the specific surface area of the samples. It was established that this parameter of the catalysts markedly decreases with increasing temperature, because the crystallinity of nanocrystalline SnO_2 particles increases. The presence of nanoparticles in the samples was verified by transmission electron microscopy and atomic force microscopy. Photooxidation reactions of the salicylic acid test molecule indicated that the catalytic effect is primarily due to the presence of nanosized tin dioxide (d = 3–6 nm). Appropriate selection of experimental conditions allows the realization of size-controlled synthesis that makes possible the preparation of nanocrystalline tin dioxide with much more advantageous photocatalytic properties than those of the reference, macrocrystalline SnO_2.

Acknowledgements

The authors thank the Hungarian National Scientific Fund (OTKA) T 034430 and M 36688 for the financial support.

References

Ansari, S.G., Boroojerdian, P., Sainkar, S.R., Karekar, R.N., Aiyer, R.C., Kulkarni, S.K., 1997. Grain size effects on H_2 gas sensitivity of thick film resistor using SnO_2 nanoparticles. Thin Solid Films 295, 271–276.

Ansari, Z.A., Ansari, S.G., Ko, T., Oh, J.-H., 2002. Effect of MoO_3 doping and grain size on SnO_2-enhancement of sensitivity and selectivity for CO and H_2 gas sensing. Sensors and Actuators B 87, 105–114.

Bartram, F., 1967. Crystallite-size determination from line broadening and spotty patterns. In: Kaelble, E.F. (Ed.), Handbook of X-rays. McGraw-Hill, New York, pp. 17.1–17.18. Chap. 17.

Chappel, S., Zaban, A., 2002. Nanoporous SnO_2 electrodes for dye-sensitized solar cells: improved cell performance by the synthesis of 18 nm SnO_2 colloids. Solar Energy Materials and Solar Cells 71, 141–152.

Cun, W., Jincai, Z., Xinming, W., Bixian, M., Guoying, S., Ping'an, P., Jiamo, F., 2002. Preparation, characterization and photocatalytic activity of nano-sized ZnO/SnO_2 coupled photocatalysts. Applied Catalysis. B, Environmental 39, 269–279.

Dékány, I., Turi, L., Tombácz, E., Fendler, J.H., 1995. Preparation of size-quantized CdS and ZnS particles in nanophase reactors provided by binary liquids adsorbed at layered silicates. Langmuir 11, 2285–2292.

Dékány, I., Turi, L., Király, Z., 1999. CdS, TiO_2 and Pd-circle nanoparticles growing in the interlamellar space of montmorillonite in binary liquids. Applied Clay Science 15, 221–239.

Dékány, I., Szücs, A., Mogyorósi, K., Király, Z., 2000. Liquid sorption and nanoparticle intercalation in layer-structured materials. Molecular Crystals and Liquid Crystals 341, 1167–1172.

Ding, Z., Zhu, H.Y., Lu, G.Q., Greenfield, P.F., 1999. Photocatalytic properties of titania pillared clays by different drying methods. Journal of Colloid and Interface Science 209, 193–199.

Hagfeldt, A., Graetzel, M., 1995. Light-induced redox reactions in nanocrystalline systems. Chemical Reviews 95, 49–68.

Jiménez, V.M., Gonzalez-Elipe, A.R., Espinos, J.P., Justo, A., Fernandez, A., 1996. Synthesis of SnO and SnO_2 nanocrystalline powders by the gas phase condensation method. Sensors and Actuators B 31, 29–32.

Jiménez, V.M., Caballero, A., Fernandez, A., Espinós, J.P., Ocana, M., González-Elipe, A.R., 1999. Structural characterization of partially amorphous SnO_2 nanoparticles by factor analysis of XAS and FT-IR spectra. Solid State Ionics 116, 117–127.

Kim, D.-W., Oh, S.-G., Lee, J.-D., 1999. Preparation of ultrafine monodispersed indium-tin oxide particles in AOT-based reverse microemulsions as nanoreactors. Langmuir 15, 1599–1603.

Kiricsi, I., Pálinkó, I., Tasi, Gy., Hannus, I., 1994. Incorporating $SnO_2 \times H_2O$ into the interlayer spacing of montmorillonite. Molecular Crystals and Liquid Crystals 244, 149–154.

Maffeis, T.G.G., Owen, G.T., Penny, M.W., Starke, T.K.H., Clark, S.A., Ferkel, H., Wilks, S.P., 2002. Nano-crystalline SnO_2 gas sensor response to O_2 and CH_4 at elevated temperature investigated by XPS. Surface Science 520, 29–34.

Mogyorósi, K., Dékany, I., Fendler, J.H., 2003. Preparation and characterization of clay mineral intercalated titanium dioxide nanoparticles. Langmuir 19, 2938–2946.

Nütz, T., Haase, M., 2000. Wet-chemical synthesis of doped nanoparticles: optical properties of oxygen-deficient and antimony-doped colloidal SnO_2. Journal of Physical Chemistry B 104, 8430–8437.

Ooka, C., Akita, S., Ohashi, Y., Horiuchi, T., Suzuki, K., Komai, S., Yoshida, H., Hattori, T., 1999. Crystallization of hydrothermally treated TiO_2 pillars in pillared montmorillonite for improvement of the photocatalytic activity. Journal of Materials Chemistry 9, 2943–2952.

Ozin, G.A., 1992. Nanochemistry: synthesis in diminishing dimensions. Advanced Materials 4, 612–649.

Richards, R., Li, W., Decker, S., Davidson, C., Koper, O., Zaikowski, A., Volodin, A., Rieker, T., Klabunde, K., 2000. Consolidation of metal oxide nanocrystals. Reactive pellets with controllable pore structure that represent a new family of porous, Inorganic Materials. Journal of the American Chemical Society 122, 4921–4925.

Salehi, A., 2002. Selectivity enhancement of indium-doped SnO_2 gas sensors. Thin Solid Films 416, 260–263.

Santos-Pena, J., Brousse, T., Sánchez, L., Morales, J., Schleich, D.M., 2000. Antimony doping effect on the electrochemical behavior of SnO_2 thin film electrodes. Journal of Power Sources 97–98, 232–234.

Serpone, N., Salinaro, A., 1999. Terminology, relative photonic efficiencies and quantum yields in heterogeneous photocatalysis: Part I. Suggested protocol (technical report). Pure and Applied Chemistry 71, 303–320.

Smith, J.D., 1970. The spectrophotometric determination of microgram amounts of tin with phenylfluorone. Analyst 95, 347–350.

Song, K.C., Kim, J.H., 1999. Preparation of nanosize tin oxide particles from water-in-oil microemulsions. Journal of Colloid and Interface Science 212, 193–196.

Sukharev, V., Kershaw, R., 1996. Concerning the role of oxygen in photocatalytic decomposition of salicylic acid in water. Journal of Photochemistry and Photobiology A, Chemistry 98, 165–169.

Vinodgopal, K., Kamat, P.V., 1995. Enhanced rates of photocatalytic degradation of an azo dye using SnO_2/TiO_2 coupled semiconductor. Environmental Science & Technology 29, 841–845.

Weller, H., 1993. Colloidal semiconductor Q-particles: chemistry in the transition region between solid state and molecules. Angewandte Chemie. International Edition in English 32, 41–53.

Yamanaka, S., Nishihara, T., Hattori, M., Suzuki, Y., 1987. Preparation and properties of titania pillared clay. Materials Chemistry and Physics 17 (1–2), 87–101.

Yumoto, H., Inoue, T., Li, S.J., Sako, T., Nishiyama, K., 1999. Application of ITO films to photocatalysis. Thin Solid Films 345, 38–41.